

Achieving High Power Density and Durability of Multilayered Swing-Structured Triboelectric Nanogenerator toward Marine Environmental Protection

Xiangyi Wang, Cuiying Ye, Pengfei Chen, Hao Pang, Chuanhui Wei, Yuxue Duan, Tao Jiang,* and Zhong Lin Wang*

Protecting marine environment is an important and urgent task to maintain marine ecological balance. As a promising blue energy harvesting technology, triboelectric nanogenerator (TENG) can provide electrical energy for marine environmental protection. Previous reported swing-structured TENGs have advantages of low driving force in low-frequency water waves and strong durability, but the space utilization and volume power density are relatively low. Here, a multilayered swing-structured TENG (MS-TENG) with low wear is designed to increase the space utilization rate, and thereby enhance the output performance. The MS-TENG generates the highest peak power density of $15.18 \text{ W m}^{-3} \text{ Hz}^{-1}$ and average power density of $3.56 \text{ W m}^{-3} \text{ Hz}^{-1}$ under water wave triggering at 0.8 Hz. By coupling the charge pumping and non-contact mode of main TENGs, the MS-TENG achieves strong performance stability, exhibiting little attenuation of electric output after 240 000 cycles. Furthermore, the MS-TENG has successfully powered a water quality detector for self-powered ballast water quality monitoring, and an application is presented about electrical dehydration of water-in-oil emulsions driven by the MS-TENG with a dehydration rate of 99.6%. This work promotes the development of high power density MS-TENG and demonstrates its application potential for self-powered marine environmental protection.

effectively alleviate the problems.^[1] Ocean contains rich, clean, and renewable energy, including water wave energy and tidal energy, which can be harvested to satisfy the power demands of infrastructures at internal port, and realize smart shipping and self-powered environmental monitoring in ocean.^[2] Triboelectric nanogenerator (TENG) has been extensively investigated in water wave energy harvesting, because of its advantages of wide material range, light weight, simple structure and high efficiency even at low frequency.^[3] Current studies demonstrate that the TENG is a promising strategy for efficiently harvesting low-frequency and irregular ocean wave energy.^[4]

To date, diverse TENG structures have been designed for water wave energy harvesting toward self-powered applications including environmental protection.^[5] A swing-structured TENG has been found to be suitable for capturing low-frequency and irregular wave energy, due to the advantages of small driving force and stable working state in low-frequency water waves.^[6]

In order to reduce material wear and improve the device durability, several approaches such as rolling friction, soft contact and non-contact are usually adopted, but the electrical outputs are relatively low.^[7] Therefore, a strategy of charge pumping has been proposed to achieve high electrical output performance.^[8]


1. Introduction

Energy shortage and environmental pollution caused by long-term use of fossil energy are two urgent problems to be solved, which make people desperately seek new renewable energy to

X. Wang, C. Ye, P. Chen, C. Wei, T. Jiang, Z. L. Wang
CAS Center for Excellence in Nanoscience
Beijing Key Laboratory of Micro-Nano Energy and Sensor
Beijing Institute of Nanoenergy and Nanosystems
Chinese Academy of Sciences
Beijing 101400, P. R. China
E-mail: jiangtao@binn.cas.cn; zhong.wang@mse.gatech.edu

X. Wang, C. Ye, P. Chen, C. Wei, T. Jiang
School of Nanoscience and Engineering
University of Chinese Academy of Sciences
Beijing 100049, P. R. China

H. Pang
School of Mechatronics Engineering
Beijing Institute of Technology
Beijing 100081, P. R. China
Y. Duan
School of Chemistry and Chemical Engineering
Guangxi University
Nanning, Guangxi 530004, P. R. China
Z. L. Wang
Georgia Institute of Technology
Atlanta, GA 30332, USA

 The ORCID identification number(s) for the author(s) of this article can be found under <https://doi.org/10.1002/adfm.202311196>

DOI: 10.1002/adfm.202311196

However, the TENGs are still suffering from low space utilization rate and low volume power density. It is very necessary to rationally design multilayered swing-structured TENG (MS-TENG) to further enhance the volume power density as well as keeping strong durability.

In ocean environment, besides wave energy harvesting, environmental protection is also a hot topic in scientific research.^[9] Since a ship relies on the injection and release of ballast water to regulate the balance of the ship, it may release contaminated seawater into clean seawater areas, which results in seawater pollution and biological invasion.^[10] The MS-TENG can be used to harvest water wave energy as well as realizing self-powered quality monitoring of ballast water, which can efficiently utilize energy and meanwhile protect ocean environment. In addition, due to the high ambient humidity in near port, the stored oil in tank depot contains some water, which reduces the purity of oil.^[11] The electrical energy generated by the MS-TENG can provide power for the electrical dehydration of water-in-oil emulsions to improve the oil purity and ensure working efficiency and service life of equipment in ocean.

Here, we design and fabricate a high volume power density and low-wear MS-TENG for efficient blue energy harvesting and self-powered marine environmental protection. Combining the multilayered structure and charge pumping strategy, the MS-TENG realizes a peak power density of $15.18 \text{ W m}^{-3} \text{ Hz}^{-1}$ and average power density of $3.56 \text{ W m}^{-3} \text{ Hz}^{-1}$ at low frequency of 0.8 Hz in water waves. Due to the soft-contact mode of the pumping TENG (P-TENG) and non-contact mode of the main TENG (M-TENG), the MS-TENG exhibits little decay in the electric outputs after 240 000 cycles. More importantly, the MS-TENG keeps high output current of 180.9 μA even at 1.8 Hz. A voltage multiplier circuit (VMC) is added between the P-TENG and S-TENG to improve the capacity of charge pumping. Moreover, the MS-TENG has been applied to power a water quality detector and implement the electrical dehydration of water-in-oil emulsions. This work provides the method of constructing high volume power density and low-wear TENG, and demonstrates the great potential in self-powered quality monitoring of ballast water and oil purification in storage depots near ports.

2. Results and Discussion

2.1. Structure Design and Working Mechanism of MS-TENG

The application scenarios of the MS-TENG network made of multiple TENG units in ocean are schematically shown in **Figure 1a**. Ocean energy can be efficiently harvested by the MS-TENG network to provide electric power for the electric dehydration of the port oil storage system (**Figure 1a(i)**) and the water quality monitoring of ballast water (**Figure 1a(ii)**), and finally realize self-powered marine environmental protection. The MS-TENG network can be placed in offshore area and the ballast water tank of the ship. The external structure of a single MS-TENG unit is schematically shown in **Figure 1b**, and the explosive view of the MS-TENG structure is presented in **Figure 1c**. The main part of the device is composed of five 3D-printed cylinders, with pumping TENG and three M-TENGs distributed in the gaps between adjacent cylinders. The second and fourth layers (gray part in the figure) are connected as a whole through the connecting cover as

a stator. The first and third layers (blue part in the figure) are connected as the rotator, equipped with copper counterweight blocks to realize the swing at the bottom. The screw on the connecting cover and the limiting slot on the bottom cover of the shell can prevent excessive swing angle of the rotator.

The P-TENG consists of the shell and the first-layer cylinder, in which rabbit hair brushes are placed inside four hollow strips on the shell. The external convex strips of the first-layer cylinder are attached by polytetrafluoroethylene (PTFE) films. The rabbit hair brushes with low frictional resistance can replenish the charges by rubbing against the PTFE films. The flexible copper electrodes manufactured by printed circuit board (PCB) technology are adhered to the inner wall of the shell to form an integrated free-standing TENG with multiple parallel connections. The three M-TENGs are all composed of the inner wall of adjacent outer cylinder and the outer wall of the inner cylinder pasted with flexible electrodes. The charges are injected through the P-TENG to create a potential difference between the pumped electrode and the induction electrode, generating induced charges on the other layer to output electric energy. It should be emphasized that the electrodes of the M-TENG are different from the flexible electrodes of the P-TENG, which are covered with 27.5 μm -thick Kapton films to prevent the air breakdown between the pumped electrode and induction electrode. To better illustrate the relationship between various parts of the MS-TENG structure and the wiring details, the side-sectional view of the MS-TENG is shown in **Figure S1** (Supporting Information). In order to avoid the effect of slot on the shaft that may wear the wires on the device durability during the operation, we use rubber materials to make protective gaskets. The photograph of the MS-TENG device is shown in **Figure S2** (Supporting Information).

Figure 1d demonstrates the basic circuit connection diagram of the MS-TENG. The alternating current (AC) output generated by the P-TENG is converted into a direct current (DC) signal by a rectifier bridge after the VMC, and the charges are pumped into the three M-TENGs. Since excessive accumulated charges may lead to dielectric breakdown, Zener diodes are used to stabilize the voltage and provide leakage channels for excessive charges. The circuit connection diagram and photograph of the VMC are shown in **Figure S3** (Supporting Information), which consists of six rectifier diodes and six ceramic capacitors. As shown in **Figure 1e**, the working principle of the MS-TENG is based on the coupling of contact electrification and electrostatic induction. Under external excitation, the rotator will swing from side to side due to the presence of counterweight blocks. For the P-TENG, the PTFE on the convex part of the rotator rubs against the rabbit hairs, generating positive charges on the rabbit hairs and negative charges on the PTFE surfaces. After swinging for a while, the negative charges on the PTFE eventually reach saturation, accompanied by the electrostatic induction. At the initial position, the PTFE strips on the rotator are aligned with one group of electrodes (**Figure 1e(i)**) and an equal amount of opposite charges are induced on the adjacent electrodes. The wobbling of the rotator under external excitation causes free electrons to flow from the left to the right electrode (**Figure 1e(ii)**). The induced current direction does not change until the PTFE becomes aligned with the left electrode (**Figure 1e(iii)**). With further swing motion, the free electrons flow in the opposite direction, leading to opposite current (**Figure 1e(iv)**). Then the alternative charge transfer between

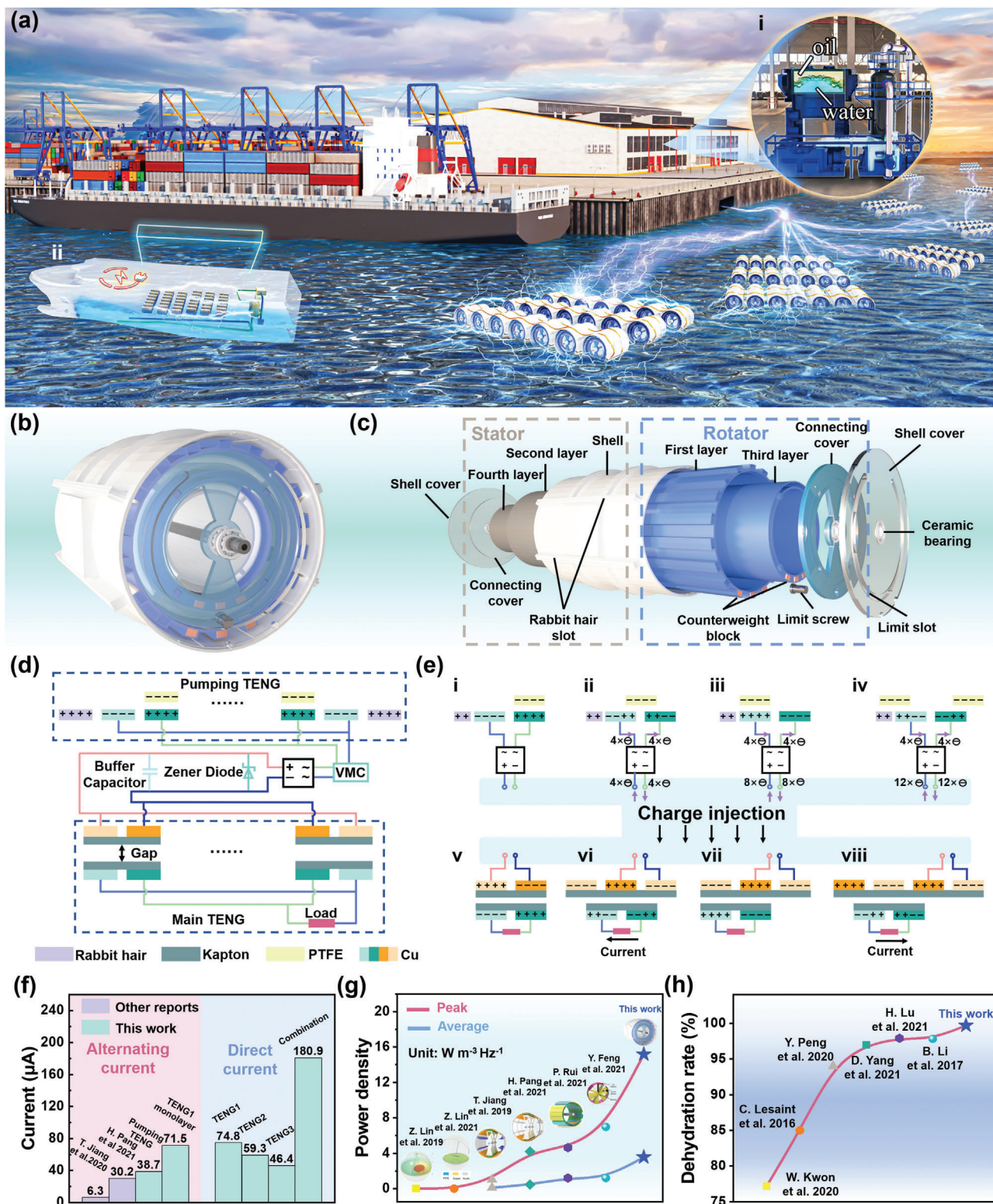


Figure 1. Structure design, working mechanism and output performance of the MS-TENG. a) Application scenario of the MS-TENG network in self-powered electrical dehydration of port oil storage system and water quality monitoring of ballast water. b) Schematic external structure of the MS-TENG unit. c) Exploded view of the MS-TENG unit. d) Schematic circuit connection diagram between the pumping TENG and main TENG of the MS-TENG. e) Working principle of the MS-TENG. f) Comparison of the output current between different parts of the MS-TENG and other swing-structured TENGs. g) Comparison of the peak and average output power densities between the MS-TENG and other swing-structured TENGs. h) Comparison of the dehydration rate of the MS-TENG with other works on the electrical dehydration.

the two electrodes of the P-TENG is rectified to DC form for continuous charge injection into the electrodes of the M-TENG. The two electrodes at the rotator side of the M-TENG obtain opposite charges with the charge injection. As the rotator swings, the induced charges on the two electrodes at the stator side will also follow the movement of the bound charges on the electrodes at the rotator. Thus, a periodic charge transfer occurs between the two electrodes at the stator side, resulting in an AC output across the load (Figure 1e(v)–(viii)).

Because the MS-TENG adopts the charge pumping strategy and has a larger electrostatic induction area, as shown in Figure 1f, the output current of the MS-TENG is much higher than that of most previous works.^[6a,c] It is worth emphasizing that the output current can reach 180.9 μA by connecting the three M-TENGs with rectifier bridges and then integrating them in parallel. The MS-TENG achieves maximum peak and average power densities of 15.18 and 3.56 $\text{W m}^{-3} \text{Hz}^{-1}$, respectively, under the water wave triggering, which are far above those of previous reported swing-structured spherical and cylindrical TENGs (Figure 1g).^[6,7c,12] The average power density can be enhanced by 242%, relative to that of previous cylindrical TENGs with the highest outputs (Figure S4, Supporting Information).^[6a,c,12a,13] The MS-TENG can provide power for the electrical dehydration of water-in-oil emulsions. Because the MS-TENG has the characteristics of high voltage and low current, compared with traditional dehydrators, the circuit will not be damaged due to short circuits caused by continuous water chains. Therefore, the applicable moisture content of the MS-TENG is much higher than that of traditional dehydrators, as shown in Figure S5 (Supporting Information). In addition, compared with other traditional dehydrators, the final dehydrating effect of the MS-TENG is excellent, as shown in Figure 1h. The final dehydration rate of the MS-TENG reaches 99.6% when the temperature is 50 $^{\circ}\text{C}$, at the initial water content of 50% and average electric field of 1000 V cm^{-1} .

2.2. Output Performance of the P-TENG

In order to maximize the output performance of the P-TENG, the structural parameter and operation conditions of the P-TENG were systematically studied, as shown in Figure 2. With the reciprocating motion of a linear motor, the rotator of the TENG will swing back and forth relative to the stator, generating electrical outputs. At the motor displacement of $s = 100 \text{ mm}$, motion acceleration of $a = 6 \text{ m}^{-1} \text{s}^2$ and pause time of $T = 250 \text{ ms}$, corresponding to the frequency of $\approx 2.0 \text{ Hz}$, the P-TENG can generate high outputs of 427 nC, 38.7 μA , and 1000 V (Figures 2a,b; Figure S6, Supporting Information). During the experiments, it was found that the rotator wall thickness (b) had an impact on the rotator swing state to affect the outputs. For comparison, two wall thicknesses of 3.5 and 5.5 mm were chosen. It can be seen from Figure 2c that with increasing the b , the output current of TENG decreases obviously. At $b = 5.5 \text{ mm}$, the output current drops to 14.7 μA . This is because larger wall thickness will increase the mass of the first-layer cylinder, raise the gravity center, and decrease the swing angle and speed, also accompanied by increased contact area with the rabbit hairs and resistance.

Then the influences of external excitation conditions on the output performance of the P-TENG were investigated, as shown

in Figure 2d,e. The output current of the P-TENG increases from 28.6 to 44.6 μA as the motor displacement increases from 50 to 150 mm at fixed motion acceleration of $6 \text{ m}^{-1} \text{s}^2$. On the other hand, when fixing the motor displacement at 100 mm, the output current of the P-TENG at various motion accelerations was measured. The P-TENG starts to swing at the acceleration of $7.5 \text{ m}^{-1} \text{s}^2$, and its output current gradually increases to 45.1 μA with decreasing the acceleration until $2.0 \text{ m}^{-1} \text{s}^2$, followed by a huge drop at $1.5 \text{ m}^{-1} \text{s}^2$. This indicates that the P-TENG in this work has a higher output under low acceleration excitation within the working area after swinging in a primary excitation, because lower acceleration can make the rotator swing more fully after swinging. So this structure is more suitable for collecting low-frequency water wave energy in the ocean. Furthermore, we defined the starting swing as the stationary-to-steady state transition of the rotator through increasing the motor acceleration at different motor displacements, and the stopping swing as the steady-to-stationary state transition of the rotator by decreasing the motion acceleration. The corresponding accelerations of starting swinging and stopping swinging at $s = 50\text{--}120 \text{ mm}$ were measured, and three working areas of the P-TENG were obtained, as shown in Figure 2f. The white, green, and blue areas represent stable swing area, chaotic area, and non-working area, respectively. The P-TENG has high outputs in the chaotic area, so it will work in the green area after one excitation makes it swing under most actual marine conditions.

Figure 2g shows the output current, peak power and average power of the P-TENG with respect to the loading resistance at an excitation frequency of 2 Hz by the linear motor. The peak power and average power are 20.0 and 3.9 mW, respectively, at the matched resistance of 20 $\text{M}\Omega$. Then the charging performance of the P-TENG to different capacitors is presented in Figure 2h, indicating that the capacitors of 22, 47, 100, and 220 μF are respectively charged to 26.6, 15.7, 8.0, and 4.1 V within 60 s. Moreover, the P-TENG exhibits strong durability, which can be observed from the long-term test results of the output voltage in Figure 2i. After continuous triggering of 160000 cycles by the linear motor, the output voltage only decreases slightly, which is attributed to the low material wear due to the soft contact of the rabbit hairs on the PTFE surface.

2.3. The Integration of the P-TENG and M-TENG

The frequency of input signals could influence the boosting effect of the VMC,^[14] so it is necessary to understand the relationship between the output frequency of P-TENG and its structural parameter, such as the grating number of PTFE strips on the rotator. Rotators with the grating numbers of 18, 24, 32, and 40 were selected for the experiments, where the number of stator electrodes varies accordingly. The frequency of the electrical signals was found to increase almost linearly with the increase in the grating number, as shown in Figure 3a. As the grating number increases, the transferred charge (Figure 3b) and output voltage (Figure S7, Supporting Information) of the P-TENG both decrease, resulting from the increase of TENG capacitance and non-ideal edge effect of electrodes.^[7b] Figure 3c shows that the output current of the P-TENG first increases and then decreases with the grating number, reaching a maximum current of 65.7 μA at

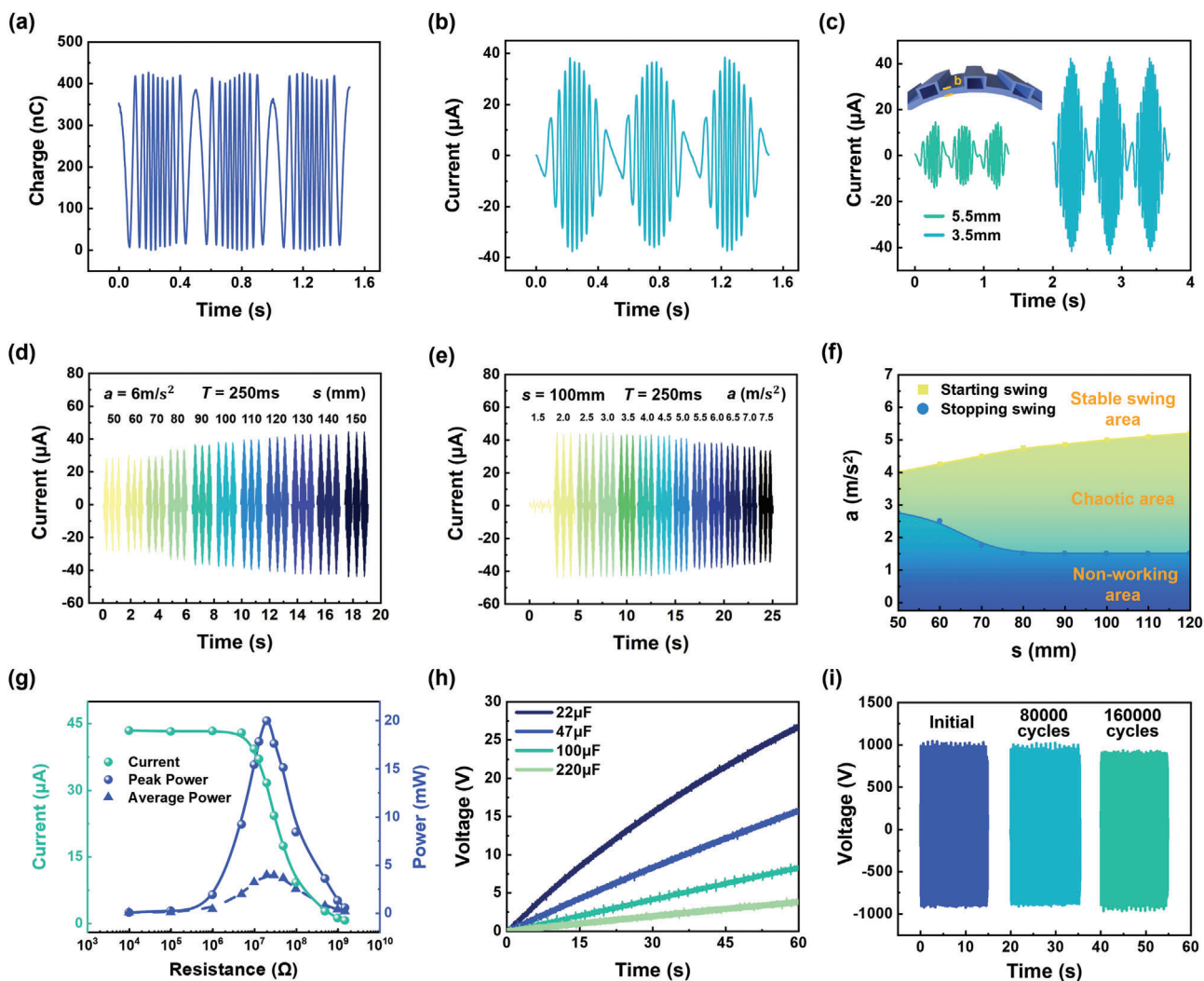


Figure 2. Output performance of the P-TENG under regular triggering. a) Transferred charge of the P-TENG at 2 Hz. b) Output current of the P-TENG at 2 Hz. c) Output current of the P-TENGs with different rotator wall thicknesses b . The cases of $b = 3.5$ and 5.5 mm were compared. d) Output current of the P-TENG at various motor displacements s at fixed motion acceleration a of $6 \text{ m}^{-1} \text{ s}^2$. e) Output current at different accelerations when fixing the motor displacement as 100 mm . f) Working areas of the P-TENG at different excitation conditions. g) Output current, peak power and average power of the P-TENG with respect to the loading resistances at 2 Hz. h) Charging voltage on different capacitors when charged by the P-TENG. i) Durability test showing the output voltage of the P-TENG in 160 000 cycles.

the grating number of 32. However, with further increasing the grating number to 40, the output current decreases to $35.7 \mu\text{A}$, which may be caused by the lower transferred charge amount and greater resistance between the rabbit hairs and more PTFE strips. Figure 3d shows the peak and average powers of the P-TENGs for different grating numbers at corresponding matched resistances. The P-TENG delivers a maximum peak power of 19.98 mW at the grating number of 18, and a maximum average power of 4.33 mW at the grating number of 32. The specific power curve at the matched resistance of $13 \text{ M}\Omega$ is shown in the inset. Figure S8 (Supporting Information) shows the peak and average powers of the P-TENGs for different grating numbers with respect to the loading resistances.

In order to better compare the charge pumping ability of the P-TENGs with different grating numbers, the P-TENGs were used to pump charges to the M-TENG1. The transferred charge

and output current of M-TENG1 were measured, as shown in Figure 3e and Figure S9 (Supporting Information). At the grating number of 18, the outputs are the highest, which are 697.9 nC and $64.6 \mu\text{A}$. Subsequently, the multiple of the VMC was adjusted to optimize the charge pumping ability of the P-TENG. When fixing the grating number as 18, the transferred charge and output current of the M-TENG1 pumped by the P-TENG using different multiples of VMCs are shown in Figure 3f and Figure S10 (Supporting Information). The results indicate that the transferred charge and output current both arrive at the maximum values when the multiple of the VMC is 6. The enlarged views of the electrical signals during one excitation period are shown in the insets. In addition, the charge pumping velocity of the P-TENG to the M-TENG1 was also explored, as shown in Figure 3g. At the frequency of 2 Hz, the charging time of pumping charges to the M-TENG1 is 6.8 s. Here, the charging time is defined as the

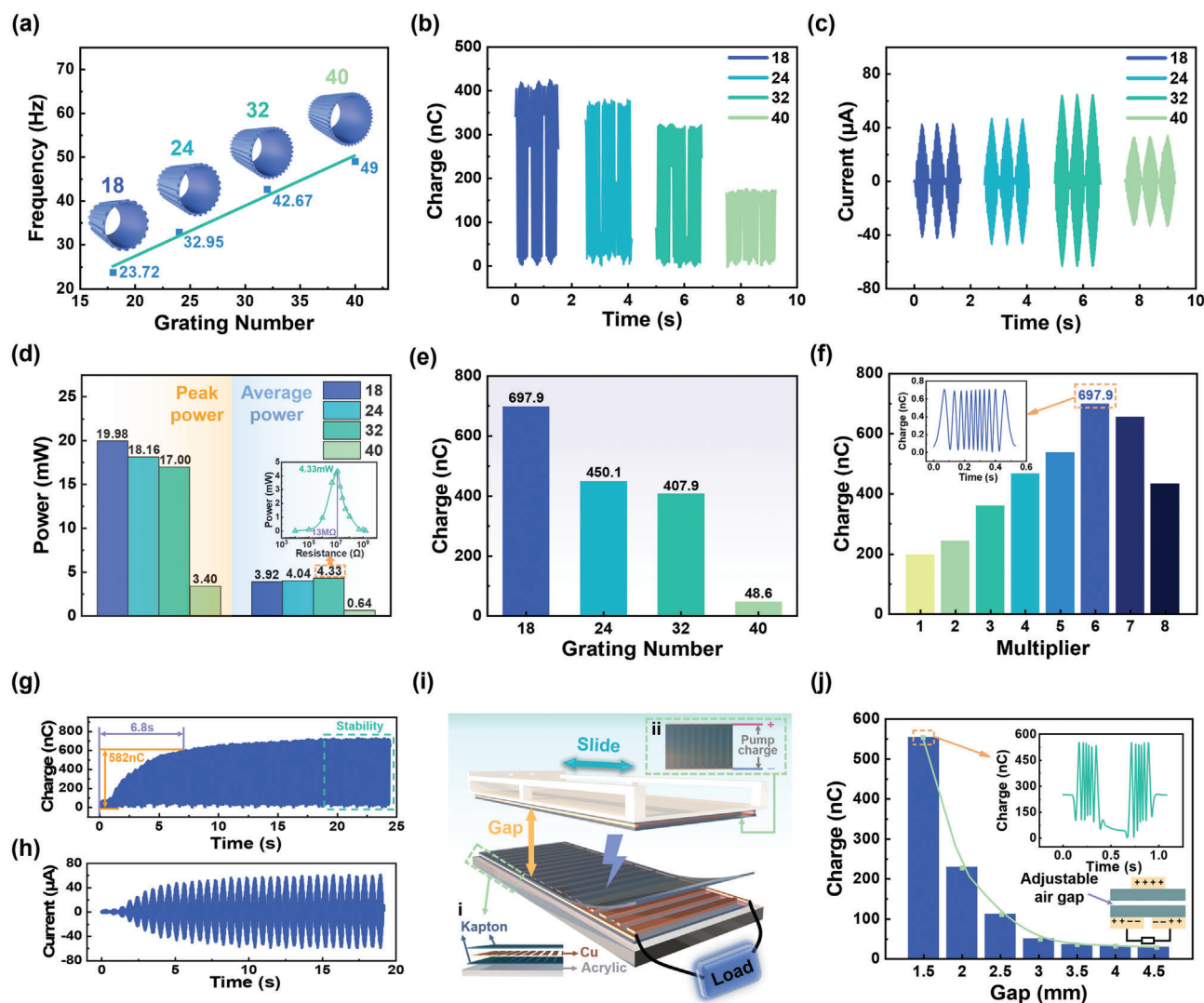


Figure 3. Integration of the P-TENG and M-TENG. a) Relationship between the frequency of electrical signals of the P-TENG and the grating number of PTFE strips on the rotor. b–d) Transferred charge, output current, peak and average powers of the P-TENGs with different grating numbers. e) Transferred charges of the M-TENG1 at various grating numbers. f) Transferred charges of the M-TENG1 at different multipliers of the VMC. g, h) Time variations of transferred charge and output current of the M-TENG1 when the multiplier of the VMC is 6. i) Schematic diagram of the platform for measuring the effect of gap distance between the pumped electrodes and the output electrodes of the M-TENG on the output performance. j) Corresponding transferred charges of the M-TENG at different gap distances between the pumped electrodes and the output electrodes.

time required to reach 80% of the maximum transferred charge amount from zero, as shown in Figure S11 (Supporting Information). At the same time, Figure 3h shows the time variation of output current of the M-TENG1 during the charging process.

In the M-TENGs, the air gap between the two electrode layers may affect the charge transfer efficiency in the electrostatic induction,^[7a,15] which can be given by the following equation:

$$\eta_{CT} = \frac{Q_{sc,final}}{\sigma S} = \frac{1}{1 + C_1(x = x_{max}) / C_2(x = x_{max})} - \frac{1}{1 + C_1(x = x_0) / C_2(x = x_0)} \quad (1)$$

where σ and S are the surface charge density and surface area of the triboelectric or pumped layer, and x is lateral separation distance. To determine the optimal gap between two layers for achieving maximum transferred charge, a simple experimental platform is built, as shown in Figure 3i. The lower layer is fixed and the upper layer reciprocates with the linear motor. The specific structure and materials of the two layers are shown in Figure 3i(i),(ii). Charges are pumped into the upper electrodes by the P-TENG, and the lower electrodes induces charges to output electrical energy through the external circuit. When the gap is smaller than 1.5 mm, the two layers will have a local contact, resulting in large, irregular motion resistance, and unstable outputs. The electrical outputs for the gap from 1.5 to 4.5 mm were measured, as shown in Figure 3j and Figure S12 (Supporting

Information), implying that the transferred charge, output current and output voltage all exhibit exponential declines with increasing the gap distance. The maximum outputs of 553.7 nC, 57.5 μ A, and 507.5 V are obtained at the gap of 1.5 mm.

2.4. Output Performance of the MS-TENG

The force analysis of the MS-TENG from the initial position to the ultimate position and then back to the initial position in half a swing cycle is shown in Figure 4a. The three M-TENGs are M-TENG1, M-TENG2, and M-TENG3 from the outside to the inside. Horizontal excitation force F_w provides an initial power, which causes the rotator to swing and the gravitational potential energy of the counterweight blocks to increase gradually. The angular velocity of the rotator (ω) has opposite direction to the angle acceleration (a) when the counterweight blocks accumulate gravitational potential energy, while the angular velocity of the rotator has the same direction as the angle acceleration when the counterweight blocks release gravitational potential energy. Therefore, the whole oscillating process is a variable speed motion, and the current produced also changes with the rotator speed. Figures 4b,c and Figure S13 (Supporting Information) show the output current, transferred charge, and output voltage of the three M-TENGs, respectively. The different outputs of the three M-TENGs are caused by the different electrostatic induction areas. The relationships between the output current, peak power and average power of the M-TENG1 and the loading resistance are shown in Figure 4d. The M-TENG can generate a maximum peak power of 34.3 mW and a maximum average power of 8.7 mW at the matched resistance of 15 M Ω . Regarding the charge decay rate of the M-TENG after disconnecting from the P-TENG, as shown in Figure S14 (Supporting Information), the output current of the M-TENG1 can still reach 29.4 μ A after 60 s of disconnection, which has a decrease of 4.2% compared to the instant of disconnection.

Furthermore, the three M-TENGs were electrically connected in parallel through the rectifier bridges to form the whole MS-TENG into which charges are pumped by the P-TENG, as shown in Figure 4e. The output current of the three M-TENGs and the whole MS-TENG after the rectification are shown in Figure 4f. The output current of the MS-TENG is nearly the superposition of the current of the three M-TENGs, reaching 180.9 μ A. The peak power and average power can reach 53.5 and 14.9 mW, respectively, under the matched resistance, as shown in Figure 4g. Then the charging performance of the MS-TENG to different capacitors was studied, as indicated in Figure 4h. The MS-TENG can charge 1, 2.2, 3.3, 6.8, and 10 mF capacitors to 4.1, 2.0, 1.4, 0.7, and 0.5 V after 60 s, respectively. The charging voltage on a 220 μ F capacitor for the three M-TENGs, MS-TENG, and the P-TENG are compared in Figure 4i. It is obvious that the MS-TENG can charge the capacitor to 17.5 V after 60 s, which is much higher than the P-TENG and three M-TENGs. It should be noted that the charging voltage of the M-TENG1 and M-TENG2, which have smaller induced electrode areas relative to the P-TENG, is higher than that of the P-TENG, implying that the multilayered structure design using charge pumping strategy possesses greater advantages. Moreover, the durability of the MS-TENG was also evaluated through measuring its output current during the continu-

ous triggering of 240 000 cycles by the linear motor, as shown in Figure 4j. The output current hardly decreases, demonstrating the strong durability of the MS-TENG, which can also be verified by the scanning electron microscope (SEM) observations on the Kapton film surfaces (Figure 4k). No material wear can be seen in the SEM images, due to the non-contact working mode in the MS-TENG with lower motion resistance. Because of the higher volume power density and excellent durability, the MS-TENG can be a promising candidate for low-frequency water wave harvesting.

To investigate the output performance of the MS-TENG in real water waves, the MS-TENG was placed in a simulated wave tank and tested. The water wave frequency range was set as 0.4–1.0 Hz and the wave height range was 2–7 cm for experimental testing. When the wave height is fixed at 7.0 cm, the trends of output voltage and output current of the P-TENG with the water wave frequency are shown in Figure 5a and Figure S15 (Supporting Information). As can be seen, the output voltage and current both first increases and then decreases with increasing the wave frequency, achieving a maximum voltage of 1330 V and a maximum current of 21.0 μ A at the frequency of 0.8 Hz. Under the optimal frequency of 0.8 Hz, the transferred charges of the P-TENG are 363.5 nC, as shown in Figure S16 (Supporting Information). Therefore, the P-TENG can still maintain a good working state under the actual water wave conditions. Meanwhile, under the same water wave conditions, the output current and output voltage of the MS-TENG with three M-TENGs in parallel were measured, shown in Figure 5b and Figure S17 (Supporting Information). Similarly, the outputs reach the highest values of 92.2 μ A and 1400 V at 0.8 Hz. On the other hand, the influence of wave height on the outputs of MS-TENG was also studied. As shown in Figure 5c and Figure S18 (Supporting Information), the output current and output voltage at the fixed frequency of 0.8 Hz both gradually increase with the increase in wave height. Under the conditions of 0.8 Hz and 7.0 cm, the output current for each M-TENG and the whole MS-TENG are compared in Figure 5d. It can be seen that the M-TENG1, M-TENG2 and M-TENG3 generate the maximum current of 38.7, 30.8, and 18.4 μ A, respectively. The three can be well superimposed due to the nearly synchronous motion of the three M-TENGs.

Subsequently, the energy conversion efficiency of the MS-TENG was evaluated, as shown in Figure S19 (Supporting Information). The impact of the water waves causes the rotator to swing from side to side, converting mechanical energy into electrical energy. Therefore, the energy conversion efficiency can be obtained by the ratio of the electrical energy output in one cycle to the difference in gravitational potential energy between the maximum oscillation state and the initial state, which is given by

$$\eta = \frac{E_{\text{ele,output}}}{E_{\text{mech,input}}} = \frac{\int I(t)^2 R dt}{(m_1 + m_3)g(h_{\text{max}} - h_0)} \times 100\% \quad (2)$$

where $I(t)$ is the output current across the loading resistor R , m_1 and m_3 are the masses of the counterweight blocks in the first and third layers, respectively, and g is the acceleration of gravity. h_0 , h_{max} are respectively the heights between the center of gravity and the bottom of the cylinder at the initial state and maximum oscillation state, which can be obtained by capturing the movement states of the swing component with a camera. The maximum

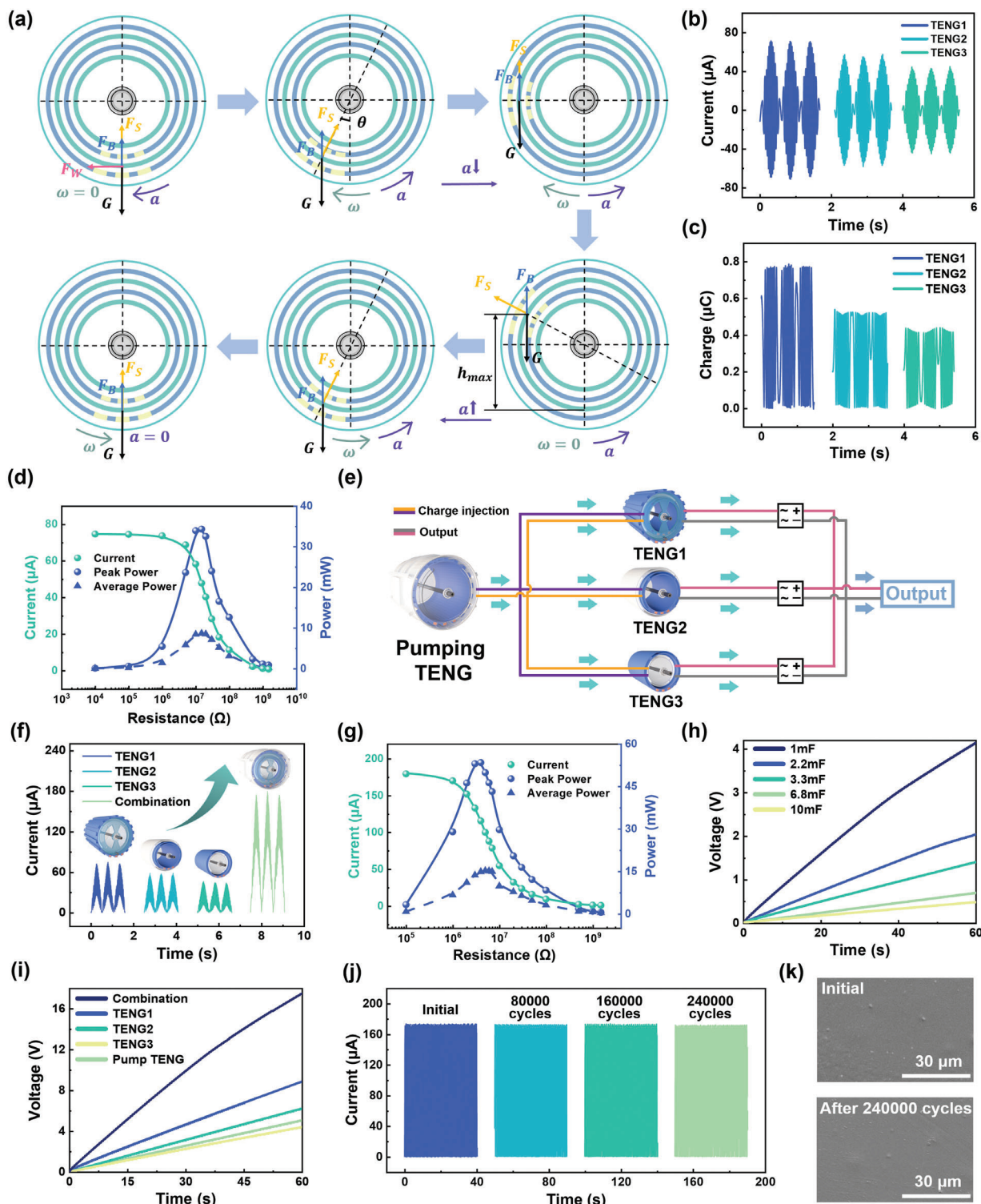


Figure 4. Output performance of the MS-TENG under regular triggering. a) Mechanical analysis of the MS-TENG at water waves. ω , a , and θ are respectively the angular velocity, angular acceleration, and rotation angle of the rotator. F_w , F_b , F_s , and G are the horizontal excitation force, buoyancy of water waves, and the bearing support force, gravity force on the rotator. b,c) Output current and transferred charge of the three M-TENGs. d) Output current, peak power and average power-resistance relationships for the M-TENG1. e) Schematic diagram of the connection between the P-TENG and M-TENGs. f) Rectified output current of the three M-TENGs and the whole MS-TENG. g) Output current, peak power and average power of the MS-TENG with respect to the resistance. h) Charging voltage on various capacitors by the MS-TENG. i) Comparison of the charging voltage on a 220 μF capacitor among the three M-TENGs, MS-TENG, and the P-TENG. j) Durability test result of the MS-TENG. k) SEM images of the Kapton film surfaces in the M-TENGs at initial state and after 240 000 working cycles.

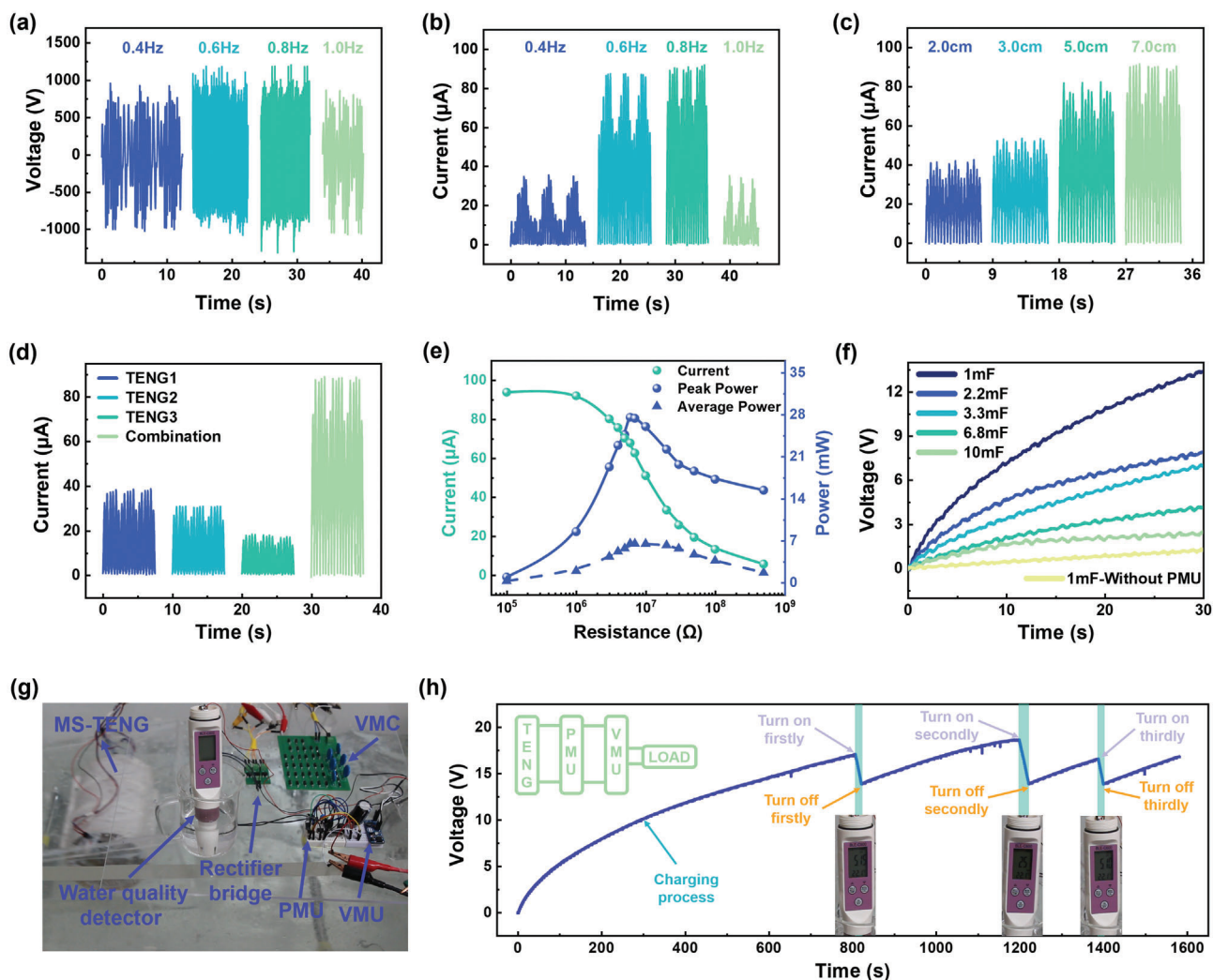


Figure 5. Output performance of the MS-TENG in the water waves and application demonstration of water quality monitoring. a,b) Output voltage of the P-TENG and output current of the MS-TENG at different water wave frequencies. The wave height is fixed as 7.0 cm, while the wave frequency varies from 0.4 to 1.0 Hz. c) Output current of the MS-TENG at various wave heights, when the wave frequency is set as 0.8 Hz. d) Comparison of the output current of each M-TENG and the whole MS-TENG under the water wave conditions of 0.8 and 7.0 cm. e) Output current, peak power and average power of the MS-TENG with respect to the resistance under the water wave conditions of 0.8 and 7.0 cm. f) Charging voltage on various capacitors charged by the MS-TENG with the PMU, as well as charging voltage on a 1 mF capacitor without the PMU. g) Photograph of the self-powered water quality monitoring system realized by the MS-TENG under the water wave triggering. h) Charging and discharging process of the 6.9 mF capacitor when powering the water quality detector by the MS-TENG and photographs of the LCD screens for showing the water quality information.

energy conversion efficiency of our MS-TENG in the water waves arrives at 24.1%. At the same time, the charging time of pumping charges to the MS-TENG was measured, as shown in Figure S20 (Supporting Information), where the output current reaches 80% of the stable current in ≈ 80 s. In addition, in Figure 5e, the output current, peak power and average power of the whole MS-TENG at different resistances under the same water wave conditions are presented. The matched resistance is 5 M Ω , and the peak and average powers are 27.6 and 6.5 mW, respectively, which correspond to power densities of 15.18 and 3.56 W m $^{-3}$ Hz $^{-1}$. We employed a power management unit (PMU) to manage the harvested energy efficiently, which consists of a buffer capacitor, a silicon-controlled rectifier and a typical buck conversion circuit. The PMU is a passive ultra-low power consumption unit, which

can operate without additional external power supply. It's completely powered by the MS-TENG. Furthermore, the ultra-low energy loss of the low power consumption diode (1N4007), silicon-controlled rectifier (SCR) and other components in the circuit can be ignored. Assisted by the PMU (Figure S21, Supporting Information), the charging speed of the MS-TENG to different capacitors is greatly enhanced, as shown in Figure 5f. With the implemented PMU, a 10 mF capacitor can be charged to 2.4 V within 30 s, while a 1 mF capacitor is only charged to 1.2 V without the PMU.

After confirming the excellent performance, the power supply capability of the water wave driven MS-TENG for ocean-related sensors toward self-powered marine environmental systems was demonstrated. An application system of water quality

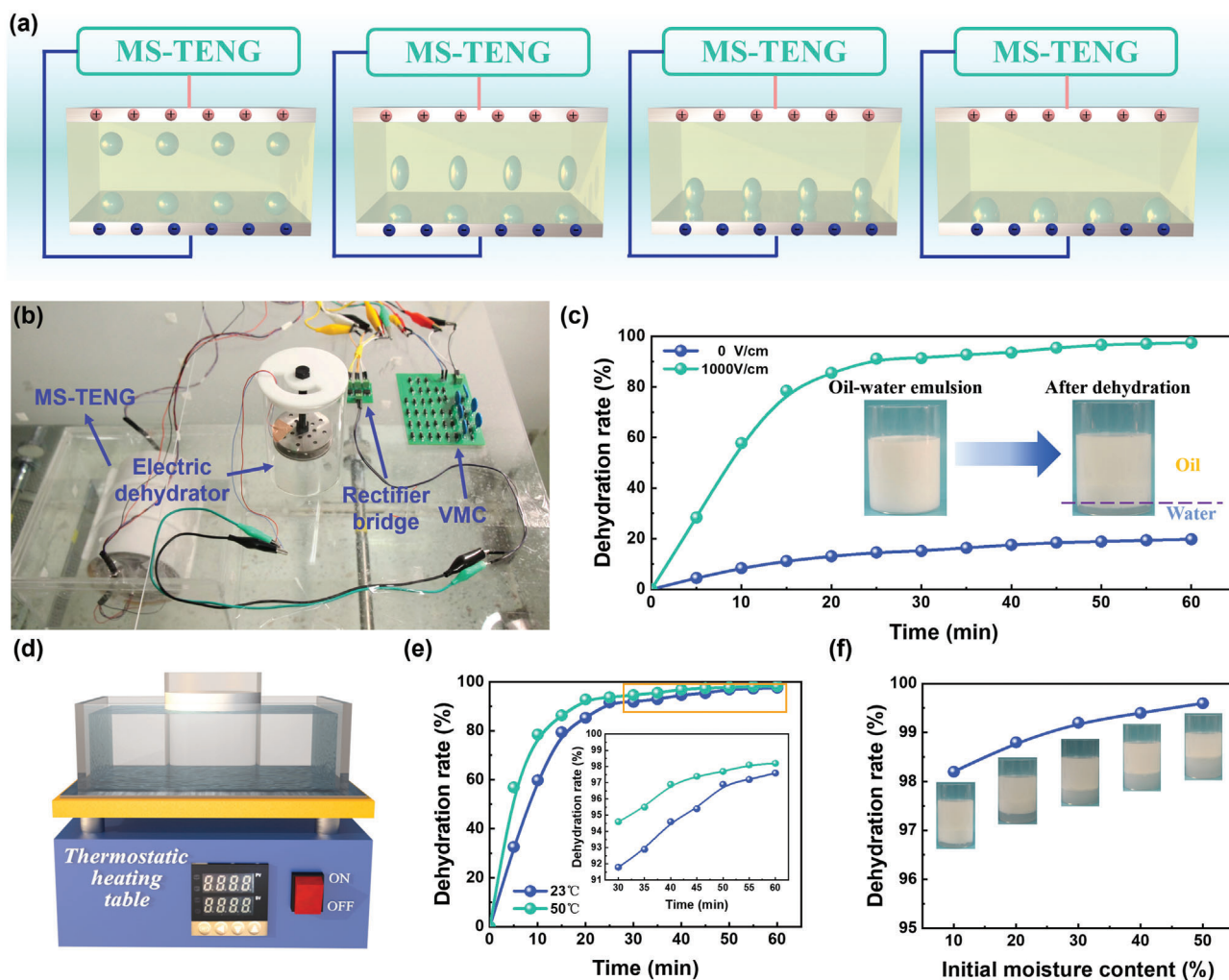


Figure 6. Application of the MS-TENG for electrical dehydration. a) Schematic motion behavior of water droplets in oil under an electric field generated by the MS-TENG. b) Photograph of the self-powered electrical dehydration system by using the MS-TENG to harvest the water wave energy. c) Enhancement effect of the dehydration rate by the MS-TENG. d) Schematic diagram of the water heating experiment setup. e) Dehydration rate-time profiles showing the dehydration process at different emulsion temperatures. f) Dehydration rate of the MS-TENG with different initial moisture contents.

monitoring of the ballast tank was simulated, as shown in Figure 5g,h. Figure 5g is the photograph of the self-powered water quality monitoring system, which is composed of the MS-TENG, rectifier bridges, VMC, PMU, a water quality detector, and a voltage management unit (VMU) (Figure S22, Supporting Information). The MS-TENG with the PMU can be used to charge a 6.9 mF capacitor, and then the energy is released through the VMU. When the VMU circuit is charged to 16 V or above, it can steadily control the release of capacitor energy to power the electrical appliances. Figure 5h and Video S1 (Supporting Information) respectively show the states of the water quality detector after charging the VMU to 17, 18, and 16 V. It is obvious that higher voltage storage before the power supply will provide a longer working time for the water quality detector. Since the ballast water quality monitoring usually occurs when the ship reaches or leaves the port, and the MS-TENGs can always collect the wave energy of ballast water while the ship is moving, the above data further proves the feasibility and practicability of the

self-powered ballast water quality monitoring system used by the MS-TENG.

2.5. Application of MS-TENG for Electrical Dehydration

Due to the high humidity of the environment near the port, the oil purity in the oil storage tank near the port is reduced. The MS-TENG can collect low-frequency water wave energy from the sea area around the port to improve the oil purity by using electrical dehydration, which ensures the working efficiency and service life of equipments. After the rectification, the MS-TENG is directly connected to the electrodes in the emulsion, as shown in Figure 6a. When the MS-TENG works, electric charges are transferred from the TENG electrodes to the dehydrator electrodes, which creates an electric field in the water-in-oil emulsion. The electric field force is mainly generated around the water droplets, and its magnitude is positively correlated with the electric field

intensity. The positively charged droplets migrate to the negative terminal, while the negatively charged droplets migrate to the positive terminal. If the droplets of the dispersed phase of the oil emulsion are charged with the same polarity, the motion direction of the droplets will be the same, but the polarized droplets with different charges will eventually coalesce due to the velocity difference between the plates. This phenomenon is called as electrophoretic coalescence. The settling velocity of water droplets in oil conforms to Stokes's Law, given by the following equation:

$$v_d = \frac{d^2 g |\rho_c - \rho_d|}{18\mu_c} \quad (3)$$

where d is the droplet diameter, g is the gravity acceleration, ρ_c is the oil density, ρ_d is the droplet density, and μ_c is the viscosity of the oil. It can be seen that the electric field can make small water droplets gather into larger water droplets, resulting in settlement. Detailed force analysis of water droplets in oil under the electric field is shown in Note S1 (Supporting Information).

The photograph of self-powered electrical dehydration system powered by the MS-TENG through harvesting the water wave energy is shown in Figure 6b. First, the effect of the electric field on the dehydration rate was examined at room temperature. Configuring an emulsion with an initial moisture content of 10%, the dehydration rate as a function of the time is shown in Figure 6c. The dehydration rate is significantly enhanced by the electric field provided by the MS-TENG compared to gravitational settling without the electric field. The dehydration process was faster in the early stage and slowed down gradually in the late stage. Video S2 (Supporting Information) demonstrates the microscopic dynamics of the emulsion in the dehydration process, directly illustrating the significant effect of the electric field compared to gravitational settling. Therefore, the dehydration rate of 5 min was defined as the dehydration speed, and the dehydration rate of 60 min was defined as the final dehydration rate. Calculations of the moisture contents and dehydration rates can be seen in Note S2 (Supporting Information).

Since the viscosity of emulsion decreases with increasing the temperature, the influence of viscosity was studied through adjusting the temperature. Comparison experiments were carried out in a water bath of 50 °C and at the room temperature of 23 °C, as shown in Figure 6d. At the same time, the experiments were carried out under the average electric field intensity of 1000 V cm⁻¹. At 50 °C, both the dehydration speed and dehydration rate are significantly increased, and the final dehydration rate can reach 98.2% after 60 min, as shown in Figure 6e. In addition, the final dehydration rates at different initial moisture contents were explored. As shown in Figure 6f, at 50 °C and 1000 V cm⁻¹, the final dehydration rate increases with the increase of initial moisture content. When the initial moisture content is 50%, the final dehydration rate reaches 99.6%. To obtain the water-in-oil emulsions, the initial moisture content of 40% was selected for the experimental demonstration of electrical dehydration by the MS-TENG, as shown in Video S3 (Supporting Information). When the three M-TENGs are connected in series, a higher voltage output will be obtained, which can reach 1550 V (Figure S23, Supporting Information). At the same electrode distance, higher voltage will cause higher electric field intensity and improve the dehydration effect. This work well demonstrated the

important application prospects of the MS-TENG in the electrical dehydration of water-in-oil emulsions toward marine environmental protection.

3. Conclusion

In summary, a multilayered swing-structured TENG with high volume power density and strong device durability was proposed for highly efficient water wave energy harvesting. Due to the sufficient space utilization for the multilayered cylindrical structure and external charge pumping, the MS-TENG generate a peak power density of 15.18 W m⁻³ Hz⁻¹ and an average power density of 3.56 W m⁻³ Hz⁻¹ under the water wave triggering of 0.8 Hz, which are respectively 2.2 times and 3 times higher than those of reported swing-structured TENG. Relying on the soft contact of the rabbit hair brushes with PTFE films in the pumping TENG and the non-contact working mode of M-TENGs, the MS-TENG needs low driving force and has excellent durability with unattenuated output current after 240 000 triggering cycles. Furthermore, the MS-TENG under the water wave triggering was successfully applied to power a water quality detector. In addition, the MS-TENG can be provide the electric field to greatly enhance the electrical dehydration effect in the water-in-oil emulsions, where the maximum dehydration rate of 99.6% realized by the water wave-driven MS-TENG demonstrates the advantage of the MS-TENG over traditional dehydrators. The present work provides an effective TENG design for large-scale blue energy harvesting to realize self-powered quality monitoring of ballast water and oil purification in storage depots near ports for final marine environmental protection.

4. Experimental Section

Fabrication of the MS-TENG Device: *Fabrication of the P-TENG:* First of all, the cylindrical shell (length: 20 cm, diameter: 15 cm, thickness: 3 mm) of the MS-TENG was manufactured using UV curing resins through 3D printing technology. Four hollow strips with a length of 19 cm and a width of 3 mm were designed to be protruding for 10 mm from the shell, and 18 cm-long and 3 mm-wide rabbit fur brushes were inserted into the hollow strips. Then, two acrylic disks, with super-lubricated ceramic bearings having an inner diameter of 6 mm and an outer diameter of 17 mm embedded in the circular holes of 17 mm, were made using a laser cutter and added to the ends of the shell. Third, the first layer of the cylinder was made by 3D printing technology (length: 18 cm, outer diameter: 13 cm, inner diameter: 12.32 cm). The outer wall with a thickness of 5 mm has protruding structures with a central angle of 9.2°. The hollowed structures with a dimension of 8 mm×5.4 mm were distributed at each interval of 10.8°, and three adjacent hollowed structures were inserted by brass material counterweight blocks of matching size. PTFE films were adhered onto the protruding surfaces with matching dimensions, and complementary electrodes were fabricated by PCB technology.

Fabrication of the M-TENGs: The second, third and fourth layers of cylinders were made by 3D printing technology (outer diameter of the second layer: 11.92 cm, inner diameter: 10.4 cm, length: 15.5 cm; outer diameter of the third layer: 10 cm, inner diameter: 8.5 cm, length: 15 cm; outer diameter of the fourth layer: 8.1 cm, inner diameter: 6.6 cm, length: 15 cm). These three layers were similar to the first layer with three matching-size brass counterweight blocks at the bottom. One end of the third layer was designed with four bumps of 4 mm × 6 mm × 6.5 mm for easy connection with the first layer as a whole through transparent UV-curable resins. The second and fourth layers were connected in the same way. The flexible

PCBs of the M-TENGs were covered with 27.5 μm -thick Kapton layers. The ultra-lubricated ceramic bearings were used between the steel shaft and the swing components, further reducing the frictional resistance.

Electric Measurements of the TENG Device: The electrical outputs of the TENG devices under the regular triggering by a linear motor (LINMOT 1100) and under the triggering of water waves generated in the previously reported standard wave tank by using the swing motion of a push plate, were measured. In the water tank, a porous pad was utilized as a wave-absorbing pad to eliminate the effects of rebound waves. The output current, transferred charges of the TENG devices and charging voltage on the capacitors were measured by a current preamplifier (Keithley 6514 System Electrometer), while the output voltage of the TENG devices were measured by the digital oscilloscope (Agilent InfiniiVision 2000X).

Measurement of the Water Cut in Oil: The moisture content was measured using an MC-016 Micromole titrator. The device uses a coulometric titration (Coulomb analysis) method with a range from 1 μg to 100 mg, a sensitivity of 0.1 μg , and an accuracy of 2 μg from 5 μg to 1 mg. In the water-in-oil emulsion, MORKE No. 3 industrial-grade white oil was selected as the oil phase, and deionized water served as the water phase. The diameter and height of the electrodehydration reaction vessel were 8 cm and 12.5 cm, respectively. The electrodehydration reaction electrode was 304-type white steel plates with a diameter of 6 cm and a thickness of 3 mm, and the diameter of the round hole on the electrode plate was 5 mm. Electrophoretic aggregation of electric droplets in an electric field was observed by a high-speed camera (FSATCAM Mini AX).

Supporting Information

Supporting Information is available from the Wiley Online Library or from the author.

Acknowledgements

X.W., C.Y., and P.C. contributed equally to this work. The research was supported by the National Key R & D Project from Minister of Science and Technology (2021YFA1201604, 2021YFA1201601), Beijing Nova Program (20220484036), Innovation Project of Ocean Science and Technology (22-3-3-hygg-18-hy), and Youth Innovation Promotion Association, CAS.

Conflict of Interest

The authors declare no conflict of interests.

Data Availability Statement

The data that support the findings of this study are available from the corresponding author upon reasonable request.

Keywords

blue energy harvesting, charge pumping, marine environmental protection, multilayered swing-structures, triboelectric nanogenerators

Received: September 15, 2023

Revised: October 8, 2023

Published online: October 22, 2023

- [1] H. L. Van Soest, M. G. J. Den Elzen, D. P. Van Vuuren, *Nat. Commun.* **2021**, *12*, 2140.
- [2] a) J. An, Z. Wang, T. Jiang, P. Chen, X. i Liang, J. Shao, J. Nie, M. Xu, Z. L. Wang, *Mater. Today* **2020**, *41*, 10; b) Z. L. Wang, *Nature* **2017**, *542*, 159; c) X. Wang, C. Zhu, M. Wu, J. Zhang, P. Chen, H. Chen, C. Jia, X. Liang, M. Xu, *Sens. Act. A. Phys.* **2022**, *344*, 113727.
- [3] a) X. i Liang, T. Jiang, G. Liu, Y. Feng, C. Zhang, Z. L. Wang, *Energy Environ. Sci.* **2020**, *13*, 277; b) X. Wang, J. Zhang, X. Liu, S. Lin, Z. L. Wang, *J. Mater. Chem. A* **2023**, *11*, 5696; c) C. Ye, D. i Liu, P. Chen, L. N. Y. Cao, X. Li, T. Jiang, Z. L. Wang, *Adv. Mater.* **2023**, *35*, 2209713.
- [4] a) X. Liang, T. Jiang, Y. Feng, P. Lu, J. An, Z. L. Wang, *Adv. Energy Mater.* **2020**, *10*, 2002123; b) S. Liu, X. Liang, P. Chen, H. Long, T. Jiang, Z. L. Wang, *Small Methods* **2023**, *7*, 2201392; c) H. Hong, X. Yang, H. Cui, D. Zheng, H. Wen, R. Huang, L. Liu, J. Duan, Q. Tang, *Energy Environ. Sci.* **2022**, *15*, 621; d) L. Liu, J. Li, Z. Guan, L. Zhao, Z. Tian, S. Jia, H. Hong, Z. He, H. Wen, R. Huang, H. Cui, W. Ou-Yang, X. Yang, *Chem. Eng. J.* **2023**, *472*, 145039; e) H. Wen, X. Yang, R. Huang, D. Zheng, J. Yuan, H. Hong, J. Duan, Y. Zi, Q. Tang, *Adv. Sci.* **2023**, *10*, 2302009; f) L. Liu, X. Yang, L. Zhao, H. Hong, H. Cui, J. Duan, Q. Yang, Q. Tang, *ACS Nano* **2021**, *15*, 9412.
- [5] a) M. Xu, T. Zhao, C. Wang, S. L. Zhang, Z. Li, X. Pan, Z. L. Wang, *ACS Nano* **2019**, *13*, 1932; b) C. Zhang, L. He, L. Zhou, O. u Yang, W. Yuan, X. Wei, Y. Liu, L. Lu, J. Wang, Z. L. Wang, *Joule* **2021**, *5*, 1613.
- [6] a) T. Jiang, H. Pang, J. An, P. J. Lu, Y. W. Feng, X. Liang, W. Zhong, Z. L. Wang, *Adv. Energy Mater.* **2020**, *10*, 2002123; b) Z. Lin, B. Zhang, Y. Xie, Z. Wu, J. Yang, Z. L. Wang, *Adv. Funct. Mater.* **2021**, *31*, 2105237; c) H. Pang, Y. Feng, J. An, P. Chen, J. Han, T. Jiang, Z. L. Wang, *Adv. Funct. Mater.* **2021**, *31*, 2106398.
- [7] a) P. Chen, Y. Luo, R. Cheng, S. Shu, J. An, A. Berbille, T. Jiang, Z. L. Wang, *Adv. Energy Mater.* **2022**, *12*, 2201813; b) P. Chen, J. An, R. Cheng, S. Shu, A. Berbille, T. Jiang, Z. L. Wang, *Energy Environ. Sci.* **2021**, *14*, 4523; c) Z. Lin, B. Zhang, H. Guo, Z. Wu, H. Zou, J. Yang, Z. L. Wang, *Nano Energy* **2019**, *64*, 103908.
- [8] a) L. Xu, T. Z. Bu, X. D. Yang, C. Zhang, Z. L. Wang, *Nano Energy* **2018**, *49*, 625; b) H. Wang, L. Xu, Y. u Bai, Z. L. Wang, *Nat. Commun.* **2020**, *11*, 4203; c) Y. u Bai, L. Xu, S. Lin, J. Luo, H. Qin, K. Han, Z. L. Wang, *Adv. Energy Mater.* **2020**, *10*, 2000605.
- [9] R. P. Schwarzenbach, T. Egli, T. B. Hofstetter, U. Von Gunten, B. Wehrli, *Annu. Rev. Env. Resour.* **2010**, *35*, 109.
- [10] M. David, S. Gollasch, L. Penko, *J. Sea Res.* **2018**, *133*, 60.
- [11] F. Li, X. Wan, J. Hong, X. Guo, M. Sun, H. Lv, H. Wang, J. Mi, J. Cheng, X. Pan, M. Xu, Z. L. Wang, *Adv. Mater. Technol.* **2022**, *7*, 2200198.
- [12] a) P. Rui, W. Zhang, P. Wang, *ACS Nano* **2021**, *15*, 6949; b) Y. Feng, X. i Liang, J. An, T. Jiang, Z. L. Wang, *Nano Energy* **2021**, *81*, 105625.
- [13] a) R. Cao, T. Zhou, B. Wang, Y. Yin, Z. Yuan, C. Li, Z. L. Wang, *ACS Nano* **2017**, *11*, 8370; b) B. Cao, P. Wang, P. Rui, X. Wei, Z. Wang, Y. Yang, X. Tu, C. Chen, Z. Wang, Z. Yang, T. Jiang, J. Cheng, Z. L. Wang, *Adv. Energy Mater.* **2022**, *12*, 2202627; c) Y. Feng, J. Han, M. Xu, X. i Liang, T. Jiang, H. Li, Z. L. Wang, *Adv. Energy Mater.* **2022**, *12*, 2103143; d) J. Han, Y. Liu, Y. Feng, T. Jiang, Z. L. Wang, *Adv. Energy Mater.* **2023**, *13*, 2203219.
- [14] a) R. Lei, S. Li, Y. Shi, P. Yang, X. Tao, H. Zhai, Z. L. Wang, X. Chen, *Adv. Energy Mater.* **2022**, *12*, 2201708; b) W. Liu, Z. Wang, G. Wang, G. Liu, J. Chen, X. Pu, Y. i Xi, X. Wang, H. Guo, C. Hu, Z. L. Wang, *Nat. Commun.* **2019**, *10*, 1426.
- [15] S. Niu, Z. L. Wang, *Nano Energy* **2015**, *14*, 161.